Synchronical pollutant degradation and H_2 production on a Ti^{3+}-doped TiO_2 visible photocatalyst with dominant (0 0 1) facets

Jinguo Wang, Peng Zhang, Xi Li, Jian Zhu, Hexing Li[*]

The Education Ministry Key Lab of Resource Chemistry, Shanghai University of Electric Power, Shanghai 200234, PR China

ARTICLE INFO

ABSTRACT

In situ Ti^{3+}-doped TiO_2 crystal in mesoporous nanosheets with dominant (0 0 1) facets was prepared by supercritical treatment of the precursor obtained from sol–gel hydrolysis of mixed $Ti(n-OC_4H_9)_4$ and TiF_4. This photocatalyst exhibited high activity in synchronical pollutant degradation and water splitting to produce H_2 under visible light irradiation owing to synergistic promoting effects. On one hand, the narrowed energy band gap resulted from Ti^{3+}-doping and the high surface area enhanced light harvest and reactant adsorption. On the other hand, the high crystallization degree accelerated electron transfer and thus, inhibited photoelectron–hole recombination. Furthermore, the exposed (0 0 1) facets with high surface energy favored the activation of reactant molecules. The photocatalytic degradation of organic pollutants promoted the H_2 production by consuming photogenerated holes, which inhibited their recombination with photoelectrons used for reducing H^+ during water splitting.

© 2013 Elsevier B.V. All rights reserved.

1. Introduction

Photocatalysis has been widely studied owing to its potential application in environmental cleaning, H_2 production and green organic synthesis. Most studies are focused on the photocatalytic degradation organic pollutants for environmental cleaning [1,2]. Recently, H_2 production *via* photocatalytic water splitting has received increasing interest due to the urgent requirement of green energy [3–5]. Since the H_2 is produced by reduction of H^+ with photoelectrons in water splitting reaction, sacrificial agents like methanol are frequently employed to inhibit the recombination with photoelectrons by consuming holes through photocatalytic oxidation of organic compounds, leading to the enhanced H_2 evolution yield [6,7]. Obviously, synchronical pollutant degradation and H_2 production are more economic because of the combination of environmental cleaning and energy production.

The photocatalyst plays a key role in determining the yield of photocatalytic pollutant degradation and/or H_2 production. To date, most studies are focused on TiO_2 photocatalysts owing to the advantages of earth abundance, low toxicity, and strong stability [8–14]. Since pure TiO_2 could be activated only by UV lights due to its big energy bandgap (3.2 eV), a great number of doped TiO_2 have been designed with the aim to achieve visible photocatalysts [15–19]. However, their applications are still limited by low amount and easy leaching of dopants [20–22]. Meanwhile, the TiO_2

morphology also greatly affects photocatalytic efficiency [23,24]. More recently, it was reported that the TiO_2 single-crystals with dominant (0 0 1) facets favor photocatalytic oxidation due to the high surface energy [25–27], and the modification with Ti^{3+} and other species could further promote photocatalytic activity [28–33].

Many methods have been employed to prepare undoped and doped TiO_2 photocatalysts, such as EISA [17], solvothermal alcoholysis [23], hydrothermal hydrolysis [26,27], sol–gel [35], and aerosol-spray [36]. Since 2003, we developed supercritical technology to prepare doped TiO_2 polycrystals with porous structure, large surface area, high crystallization degree, and strong interaction between TiO_2 and dopants, leading to the enhanced activity and durability in photocatalysis under visible light irradiation [15,37,38]. As the progress in this research, we reported here for the first time the supercritical preparation of *in situ* Ti^{3+}-doped TiO_2 single-crystal in mesoporous nanosheets with dominant (0 0 1) facets, which exhibited high activity in synchronical degradation of organic pollutants and H_2 production under visible light irradiation. Meanwhile, the promoting effect of photocatalytic pollutant degradation on H_2 evolution was also examined and discussed.

2. Experimental

2.1. Sample preparation

The TiO_2 sample was prepared under supercritical conditions. In a typical run of synthesis, 2.5 mL dilute HNO_3 solution (1:5, V/V) was dropwised into 50 mL solution containing $Ti(n-OC_4H_9)_4$ and

* Corresponding author. Fax: +86 21 64322272.
  E-mail address: HeXing-Li@shnu.edu.cn (H. Li).

TiF$_4$ with molar ratio of 0.50 previously dissolved in 40 mL alcohol at 40 °C. After stirring for 1 h, the gel was aged at 40 °C for 72 h and then transferred into to a 500 mL autoclave containing 250 mL ethanol, followed by treating for 2 h under supercritical conditions at a given temperature (240–280 °C). After being degassed and cooled down to room temperature, the solid product was washed with ethanol and distilled water, followed by drying at 80 °C for 6 h. The as-received samples were denoted as TiO$_2$-X, where X refers to the supercritical temperature (°C).

For comparison, the single-crystal TiO$_2$ was also synthesized according to the method reported elsewhere [27] and denoted as TiO$_2$-Ref. Briefly, 5.0 mL tetrabutyl titanate and 0.60 mL HF aqueous solution (47%) were mixed, and then transferred into a 15 mL Teflon autoclave. After being treated at 180 °C for 24 h, the white powder was washed with ethanol and distilled water for three times, followed by drying at 80 °C for 8 h.

For the photocatalytic water splitting, the Pt/TiO$_2$ with 1.0 wt% Pt loading was prepared according to the following procedure reported previously [34]. 50 mg TiO$_2$ was immerged in a solution containing 1.3 mg H$_2$PtCl$_6$·6H$_2$O, 60 mL distilled water and 20 mL methanol, followed by irradiating with a 300 W xenon lamp for 45 min at 25 °C under gentle stirring. The as-received Pt/TiO$_2$ was collected by centrifuging, followed by washing with ethanol and distilled water for three times, and finally dried at 80 °C for 6 h.

2.2. Characterization

The crystal structure and morphology were determined using X-ray diffraction (XRD, D/MAX-2000 with CuKα radiation), field emission scanning electron microscopy (FESEM, HITACHI S4800), transmission electron microscopy (TEM) and selected area electron diffraction (SAED) on a JEM-2100. The surface electronic state was analyzed by X-ray photoelectron spectroscopy (XPS, Perkin-Elmer PHI 5000). All the binding energy values were calibrated by using C$_{1S}$ = 284.6 eV as the reference. Nitrogen adsorption–desorption isotherms were measured at −196 °C using their surface area (Quantachrome NOVA 4000e), from which the specific surface area (S_{BET}), pore volume (V_P) and average pore diameter (D_P) were calculated by applying Brunauer–Emmett–Teller (BET) and Barret–Joyner–Halender (BJH) methods on the desorption branches. Raman spectra, photoluminescence spectroscopy (PLS), and UV–vis diffuse reflectance spectra (UV–vis DRS) were collected on Dilor Super LabRam II, Varian Cary-Eclipse 500, and MC-2530, respectively. The low temperature electron paramagnetic resonance (EPR) spectra were recorded on a BRIAN e-112 at room temperature.

2.3. Activity test

Synchronical photocatalytic degradation of organic pollutants and water splitting under visible light irradiation were carried out at 30 °C in a photocatalytic hydrogen evolution reactor containing 50 mg catalyst coated with 1.0 wt% Pt and 100 mL aqueous solution containing 20 mg/L organic pollutant, including methylene blue (MB), methyl orange (MO), rhodamine B (RhB), or 4-chlorophenol (4-CP). The mixture was stirred at 30 °C for 30 min in dark in order to reach the adsorption–desorption equilibrium. The photocatalysis was initiated by irradiating the reaction system with a 300 W xenon lamp located at 30 cm away from the solution surface. All lights with wavelength (λ) shorter than 420 nm were removed by a glass filter (JB-420). After reaction for 3 h, the amount of hydrogen evolved was determined on a gas chromatograph (GC-2010 shimadzu, N$_2$ carrier) equipped with a thermal conductivity detector (TCD2-C), while the degradation yield was calculated based on the unreacted organic pollutant, which could be measured by light absorbance on a UV spectrophotometer (UV-7504/PC) at the
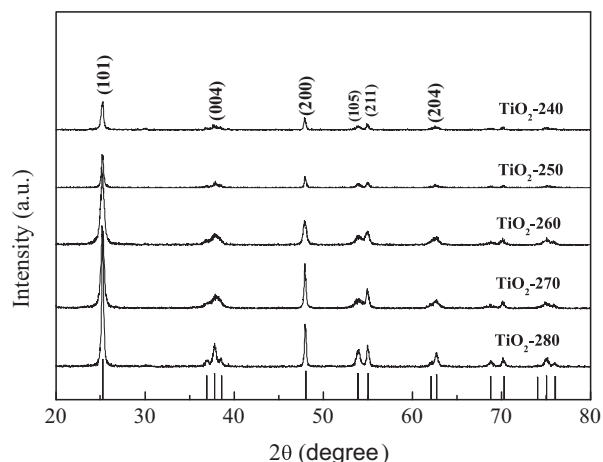

Fig. 1. XRD patterns of different TiO$_2$ samples.

characteristic wavelength corresponding to each organic compound. Preliminary tests demonstrated that the H$_2$ evolution and the degradation of organic pollutants in the absence of either the photocatalyst or the light irradiation could be neglected in comparison with those obtained *via* photocatalysis. The photocatalytic activity test under UV light irradiation was conducted in the similar way to that under visible light irradiation by using four 3.0 W UV-LEDs lamps with characteristic λ of 365 nm located at 1.0 cm away from the solution surface. The reproducibility checked by repeating each test at least three times and was found to be within acceptable limits ($\pm 5\%$).

## 3. Results and discussion

3.1. Structural characteristics

The XPS spectrum (Fig. S1) demonstrated the absence of carbon doping in TiO$_2$-260 and TiO$_2$-Ref since no significant signals characteristic of carbon species in either the Ti—C or the Ti—O—C bond were observed around binding energies of 281.2 eV and 288.6 eV, respectively [28]. The XRD patterns in Fig. 1 demonstrated that all the as-prepared TiO$_2$ samples were present in anatase phase, corresponding to 2θ of 25.8°, 37.7°, 47.8° and 55.0° indicative of (1 0 1), (0 0 4), (2 0 0) and (2 1 1) diffractions (JCPDS No. 12-1272) [19]. The crystallization degree increased gradually with the increase of supercritical temperature. Taking into account that the exposed (0 0 1) facets were formed due to the deformation growth of anatase TiO$_2$ crystal from octahedron to decahedron (see Scheme 1) [39], the percentage of exposed (0 0 1) facets increased if the up and down crystal growth was retarded or inhibited. According to Scherrer equation, the broad peak (*i.e.*, the enhanced half-height width) indicative of (0 0 4) diffraction represented the decreased crystallite size along [0 0 1] axis vertical to (0 0 1), corresponding to small "*h*" in Scheme 1, implying the enhanced percentage of exposed (0 0 1) facets. Meanwhile, the enhanced intensity of (1 0 1) peak referred to increased crystallite size along [1 0 1] axis vertical to (1 0 1), corresponding to the "*m*" in Scheme 1, which also suggested the enhanced percentage of exposed (0 0 1) facets. Thus, the percentage of exposed (0 0 1) facets could be estimated from the ratio between peak intensities of (0 0 4) and (1 0 1). As shown in Table 1, the percentage of exposed (0 0 1) facets first increased with the supercritical temperature increasing from 240 to 260 °C and then decreased gradually with the supercritical temperature further increasing.

As shown in Fig. 2, both FESEM and TEM images revealed that the TiO$_2$-260 was present in nanosheets with average length of

Table 1
Physical structural parameters of different TiO_2 samples.

Sample	S_{BET} (m^2/g)	V_P (cm^3/g)	D_P (nm)	Thickness (nm)	Length (nm)	Exposed (0 0 1) facets (%)
TiO$_2$-Ref	96	0.39	16	6	40	77
TiO$_2$-240	40	0.090	2.1	40	140	56
TiO$_2$-250	48	0.11	2.1	35	120	58
TiO$_2$-260	51	0.17	2.3	30	120	65
TiO$_2$-270	51	0.17	2.2	30	100	63
TiO$_2$-280	50	0.16	2.0	35	80	57
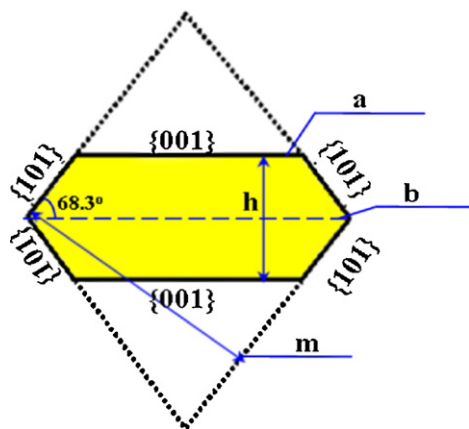
Scheme 1. Model illustrating the formation of exposed (0 0 1) facets in anatase TiO_2 crystal through deformation growth from octahedron to decahedron.

120–150 nm and thickness around 20 nm. Meanwhile, the HRTEM images and SAED patterns also confirmed that the TiO$_2$-260 displayed exposed (0 0 1) facets. The FESEM images in Fig. 3 revealed that TiO$_2$ nanorods were obtained at low supercritical temperature (240 °C), which gradually transformed into nanosheets with the increase of supercritical temperature to 260 °C owing to the orientation gathering of TiO$_2$ nanoparticles, together with the Ostwald

ripening process. Further increasing supercritical temperature to 280 °C caused stack of nanosheets, corresponding to the enhanced thickness. The average length and thickness of TiO$_2$ obtained at different supercritical temperature were calculated according to FESEM morphologies (see Table 1). Taking into account that the top and bottom surfaces represented (0 0 1) facets while the side-surfaces corresponded to (1 0 1) facets, the change in percentage of exposed (0 0 1) facets with the supercritical temperature could be explained by considering the orientation growth of TiO$_2$ crystal. At low supercritical temperature, the TiO$_2$ crystal in nanorods with high thickness and low width displayed low percentage of exposed (0 0 1) facets due to the low areas of top and bottom surfaces. The TiO$_2$ nanosheets obtained at high supercritical temperature displayed large areas of top and bottom surfaces, corresponding to high percentage of exposed (0 0 1) facets. However, further increase in supercritical temperature resulted in stack of TiO$_2$ nanosheets, leading to decreased percentage of exposed (0 0 1) facets.

The XRD pattern, TEM and HRTEM images (Fig. S2) revealed that the TiO$_2$-Ref was also present in anatase TiO$_2$ single crystal in the form of nanosheets. Table 1 demonstrates that TiO$_2$-Ref displayed even higher percentage of exposed (0 0 1) facets than the TiO$_2$-260 due to the use of HF acid since the F$^-$ ions might be strongly adsorbed on the (0 0 1) facets, which could reduce the surface energy of high-reactive (0 0 1) facets and thus retard the crystal growth along [0 0 1] axis, leading to the truncation of octahedron toward decahedron with dominant (0 0 1) facets [26].
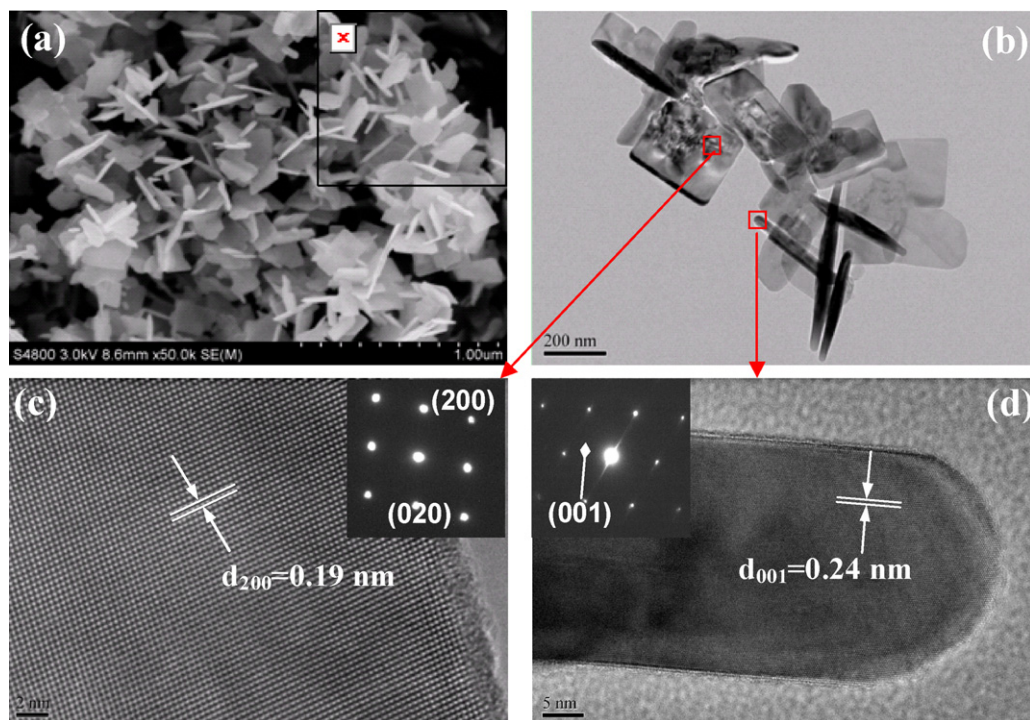

Fig. 2. (a) FESEM and (b, c, and d) images of TiO$_2$-260. The insets in (c) and (d) are SAED images.
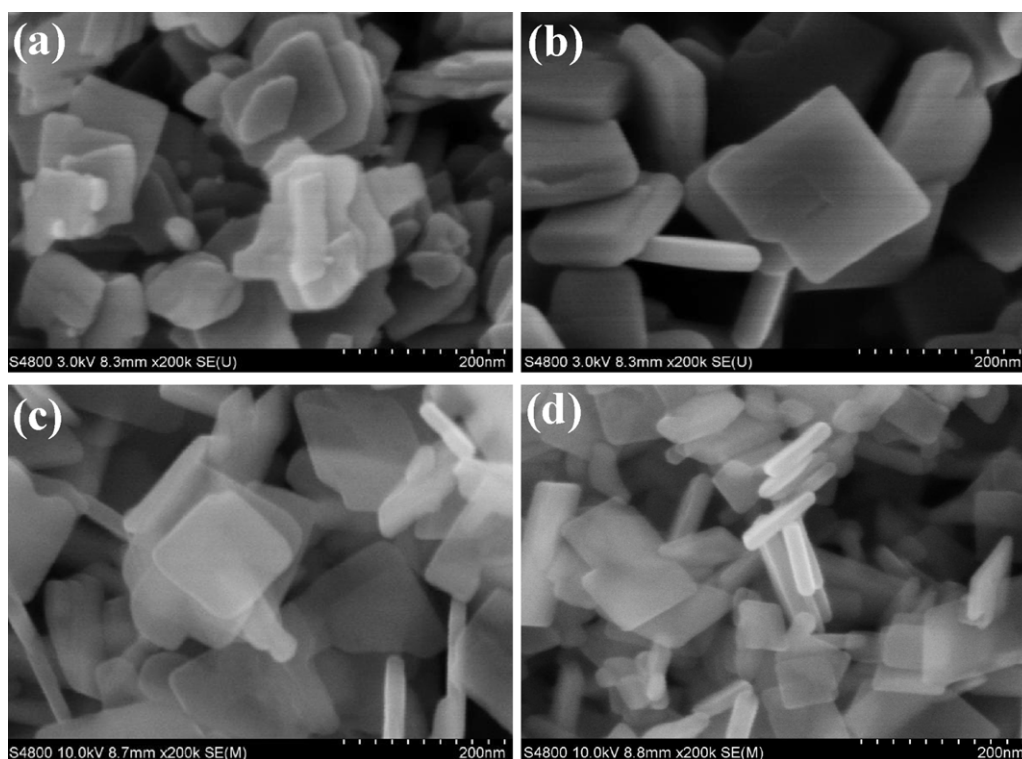
Fig. 3. FESEM images of (a) TiO_2-240, (b) TiO_2-250, (c) TiO_2-270, and (d) TiO_2-280.

Fig. 4 demonstrates that all the TiO_2 samples obtained at different supercritical temperatures (240–280 °C) displayed type IV nitrogen adsorption–desorption isotherms with hysteresis loops indicative of the mesoporous structure with narrow pore size distribution centered around 2.1 nm. These mesopores were constructed by gathering of TiO_2 nanoparticles into nanosheets [40]. The TiO_2-Ref showed two kinds of porous structures. The small pores with average diameter around 2.1 nm might be constructed by gathering of TiO_2 nanoparticles into nanospheres while the large pores with average diameter around 18 nm were resulted from agglomeration of TiO_2 nanospheres. Based on nitrogen adsorption–desorption isotherms, the S_{BET}, V_P and D_P could be calculated by using BET and BJH models, respectively. As shown in Table 1, the S_{BET}, V_P and D_P increased gradually with the increase of supercritical temperature from 240 to 260 °C owing to the growth of mesoporous TiO_2

nanosheets. However, further increase in supercritical temperature resulted in slight decrease in S_{BET}, V_P and D_P, which could mainly be attributed to the stack of TiO_2 nanosheets.

As shown in Fig. 5, the UV–vis DRS spectra demonstrated that the TiO_2-Ref displayed no significant spectral response in visible area, obviously due to the big energy band gap of anatase (3.2 eV). However, all the TiO_2 samples obtained at different supercritical temperatures (240–280 °C) exhibited remarkable light absorbance in visible region, possibly owing to *in situ* Ti^{3+}-doped TiO_2 and oxygen vacancies [41–44], which could be confirmed by EPR spectrum in Fig. 6, corresponding to the strong signals around $g = 1.95$ and $g = 2.00$, respectively [29,30,45,46]. No significant signal indicative of surface Ti^{3+} was observed at g of 2.02 due to the surface oxidation. Meanwhile, the Raman spectra in Fig. 7 further confirmed the presence of more oxygen vacancies in the TiO_2-260 than that
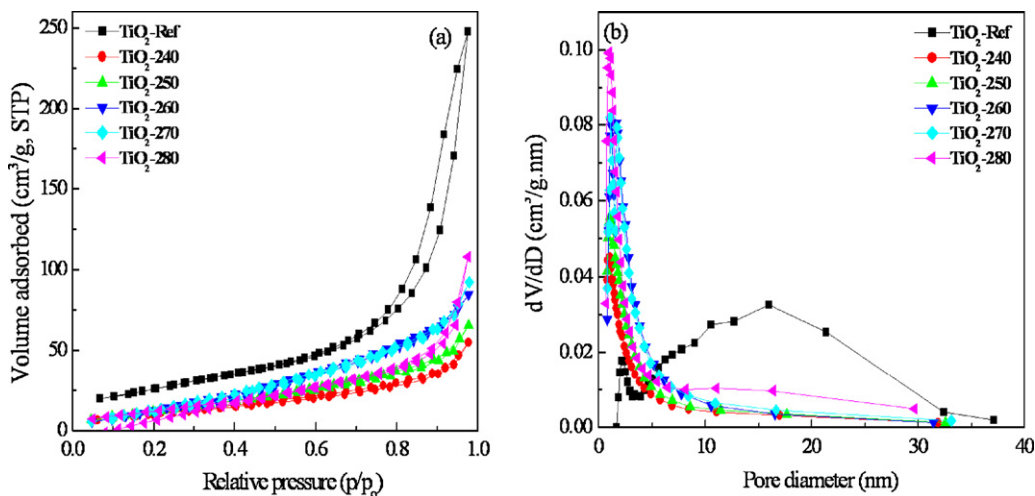

Fig. 4. (a) N_2 adsorption–desorption isotherms and (b) the corresponding pore-size distribution curves of different TiO_2 samples.
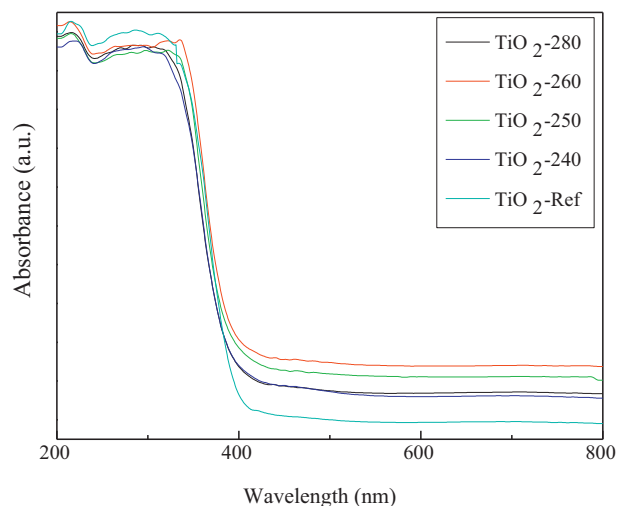
Fig. 5. UV–vis DRS spectra of different TiO$_2$ samples. (For interpretation of the references to color in this figure legend, the reader is referred to the web version of this article.)
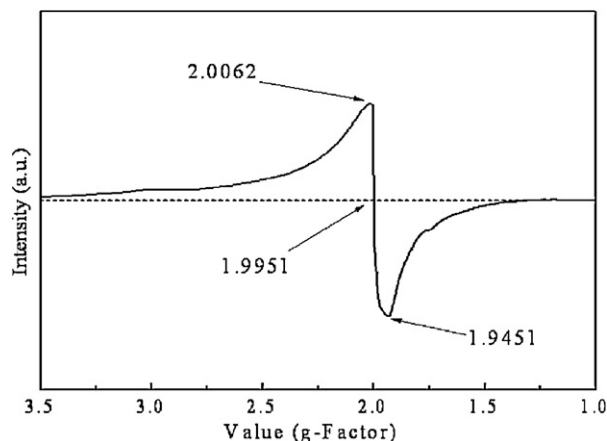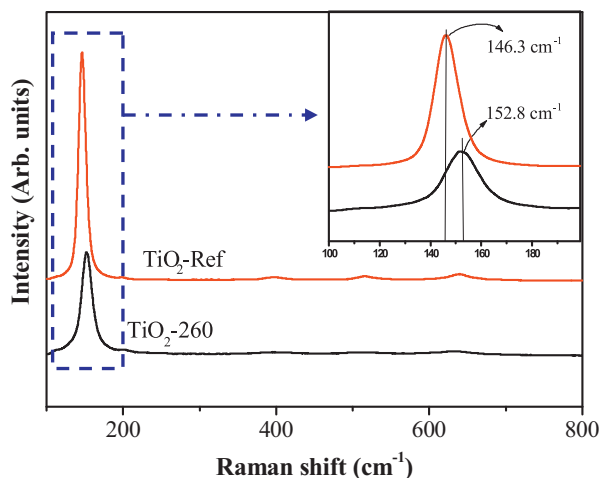

Fig. 6. Representative EPR spectrum of TiO$_2$-260.

Fig. 7. Raman spectra of TiO$_2$-Ref and TiO$_2$-260 samples. (For interpretation of the references to color in this figure legend, the reader is referred to the web version of this article.)
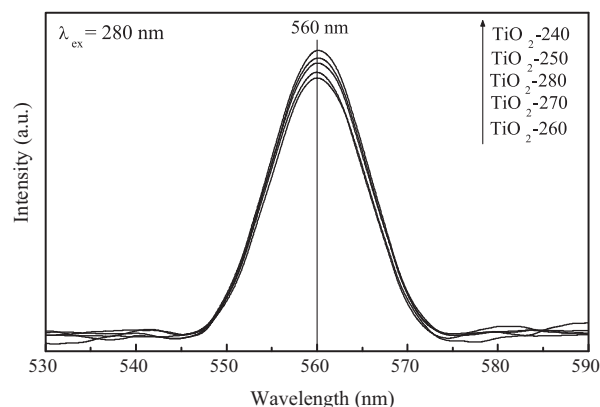

Fig. 8. PLS spectra of different TiO$_2$ samples.

in the TiO$_2$-Ref, corresponding to the positive shift of the principal peak position by 6.5 cm^{-1} [35]. The Ti^{3+} species were generated from reduction of Ti^{4+} by organic substances and/or residues under supercritical conditions and the *in situ* Ti^{3+}-doped TiO$_2$ displayed oxygen vacancies due to the replacement of Ti^{4+} by Ti^{3+} in the TiO$_2$ lattice. Meanwhile, the (0 0 1) facet contained more oxygen vacancies than the (1 0 1) facet since each Ti in the (0 0 1) facet coordinated with 5 oxygen atoms while each Ti in the (1 0 1) facet coordinated with either 5 or 6 oxygen atoms in the probability around 50% to 50% [25,26]. The presence of Ti^{3+}-dopants and the oxygen vacancies in the TiO$_2$ resulted in some new energy levels below the conduction band [44,47,48], leading to the spectral response in visible area. Fig. 5 also demonstrates that, the light absorbance in visible area increased with the increase of supercritical temperature from 240 to 260 °C, which could be attributed to the enhanced Ti^{3+}-dopants, oxygen vacancies and percentage of (0 0 1) facets. However, further increase in the supercritical temperature resulted in the decreased absorbance for visible lights, possibly due to the decrease in the percentage of exposed (0 0 1) facets (see Table 1).

The PLS spectra in Fig. 8 revealed that the intensity of PL emission around 560 nm decreased with the increase of supercritical temperature from 240 to 260 °C, corresponding to the reduced recombination rate between photoelectrons and holes [49]. On one hand, the enhanced crystallization degree facilitated the transfer of photoelectrons, which diminished their recombination with photogenerated holes. On the other hand, the oxygen vacancies increased with the supercritical temperature, which could capture photoelectrons and thus, inhibited their recombination with holes. The TiO$_2$ obtained at very high supercritical temperature (280 °C) displayed higher recombination rate between photoelectrons and holes due to the decrease in oxygen vacancies, taking into account that the crystallization degree remained unchanged.

3.2. Photocatalytic performances

Synchronical photocatalytic degradation of organic pollutant and water splitting under visible light irradiation (>420 nm) was used to evaluate activities of different TiO$_2$ samples. The Pt/TiO$_2$ was used instead of pure TiO$_2$ since the presence of noble metal on TiO$_2$ surface could facilitate the electron transfer, which might suppress photoelectron–hole recombination. Meanwhile, the presence of Pt metal could also reduce the H$_2$ production overpotential and retard the O$_2$–H$_2$ reverse reaction [34]. As shown in Fig. 9, the rate of hydrogen evolution from pure water splitting was very low. The addition of organic pollutant could significantly promote water splitting, leading to the enhanced H$_2$ evolution. As well known, the H$_2$ production from water splitting was driven by reduction of H$^+$ in
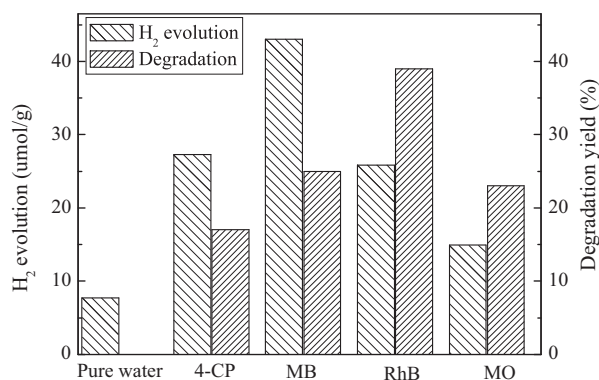
Fig. 9. Synchronical water splitting and degradation of organic pollutant (20 mg/L) on TiO$_2$-260 photocatalyst irradiated with visible lights (>420 nm) for 3 h.

water with photoelectrons [1]. The presence of organic pollutants could promote water splitting reaction since the holes generated from TiO$_2$ semiconductor under light irradiation could be greatly consumed during photocatalytic degradation of organic pollutants, which could effectively inhibit their recombination with photoelectrons. Meanwhile, Fig. 9 also demonstrates that the nature of organic pollutants played a key role in determining water splitting rate to produce H$_2$. The MB degradation displayed the strongest promoting effect on water splitting in comparison, corresponding to the highest H$_2$ evolution. 4-CP showed lower H$_2$ evolution rate than MB due to the lower degradation rate. Although the higher degradation rate, RhB still exhibited lower H$_2$ evolution rate than MB, suggesting that very rapid degradation of organic pollutants was also harmful for H$_2$ evolution since partial photoelectrons might also be consumed during degradation of organic compounds. Interestingly, although the MO showed lower degradation yield than the RhB, it still exhibited lower H$_2$ evolution rate possibly due to the different degradation mechanism. According to our previous studies [49], RhB degradation was mainly driven by photogenerated holes while MO degradation was initially started by photoelectrons. Thus, the MO degradation competed with the water splitting for consuming photoelectrons, which might retard the water splitting.

Fig. 10 shows the degradation yield and H$_2$ evolution amount in synchronical photocatalytic degradation of MB and water splitting on different TiO$_2$ photocatalysts irradiated with visible lights (>420 nm). The TiO$_2$-Ref and P25 TiO$_2$ displayed no significant activity since it could not be activated by visible lights due to the big energy band gap (3.2 eV). With the increase of supercritical
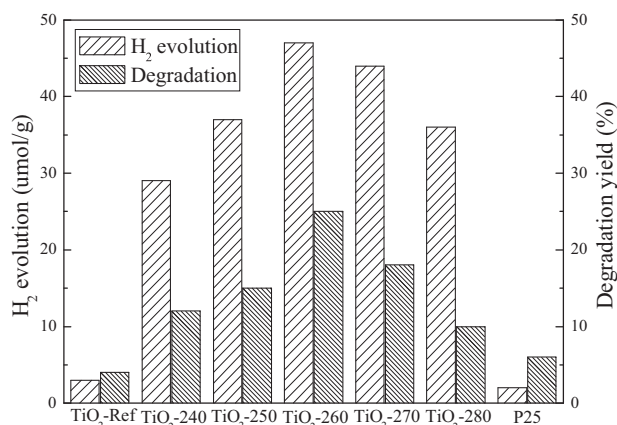
temperature, both the MB degradation rate and H$_2$ evolution rate of the as-prepared TiO$_2$ increased owing to the enhancement of crystallization degree, surface area and exposed (0 0 1) facets. The increase in surface area due to transformation from nanorods to mesoporous nanosheets could promote light harvesting and also facilitate diffusion and adsorption of reactant molecules [15]. Meanwhile, the enhanced exposed (0 0 1) facets also promoted the photocatalytic oxidations owing to the high surface energy which favored the activation of reactant molecules [26]. Besides, the (0 0 1) facet contained more oxygen vacancies than the (1 0 1) facet [25,26], which could inhibit the photoelectron–hole recombination by capturing photoelectrons and thus, promote the photocatalytic oxidations. In addition, the increase in Ti^{3+} dopants and oxygen vacancies could promote the activation of TiO$_2$ by visible lights [41–43], which also favored H$_2$ production from photocatalytic water splitting [44]. Furthermore, the high crystallization degree facilitated the photoelectrons transfer, which could reduce the recombination rate between photoelectrons and holes, leading to the enhanced quantum efficiency in photocatalysis[48]. However, very high supercritical temperature (>270 °C) was harmful for the activity of TiO$_2$ in both the MB degradation and the water splitting, which could be mainly attributed to the decrease in S_{BET}, V_P, D_P and exposed (0 0 1) facets due to the agglomeration and stack of TiO$_2$ nanosheets.

According to the photocatalytic activity test under UV light irradiation (see Fig. S3), the TiO$_2$-Ref displayed higher degradation yield and lower H$_2$ evolution rate than the TiO$_2$-260, suggesting that the exposed (0 0 1) facets favored photocatalytic oxidation of organic compounds and unfavored photocatalytic reduction of H$^+$. The P25 TiO$_2$ displayed higher H$_2$ evolution efficiency than the TiO$_2$-260, possibly owing to the presence of heterojunctions formed between anatase and rutile, which facilitated the photoelectron transfer and thus inhibited photoelectron–hole recombination. However, the P25 TiO$_2$ exhibited lower photocatalytic degradation yield than either the TiO$_2$-260 or the TiO$_2$-Ref possibly due to the absence of exposed (0 0 1) facets.

4. Conclusions

This work developed a facile approach for preparing single-crystal TiO$_2$ in mesoporous nanosheets with dominant (0 0 1) facets by supercritical technology, which could be activated by visible lights owing to *in situ* Ti^{3+}-doping, leading to the narrow band gap by forming intermediate energy levels and oxygen vacancies. This photocatalyst displayed high activity in synchronical degradation of organic pollutants and water splitting to produce H$_2$ owing to the enhanced light harvesting ability, facilitated diffusion and adsorption of reactant molecules, reduced recombination between photoelectrons and holes, and dominant (0 0 1) facets. The photocatalytic pollutant degradation greatly promoted water splitting, which supplied a powerful way in synchronical environmental cleaning and H$_2$ production.

Fig. 10. Efficiencies of different TiO$_2$ photocatalysts in synchronical water splitting and MB (20 mg/L) degradation under irradiation of visible lights (>420 nm) for 3 h.

Appendix A. Supplementary data

Supplementary data associated with this article can be found, in the online version, at doi:10.1016/j.apcatb.2013.01.006.

References

[1] A. Fujishima, K. Honda, Nature 238 (1972) 37.
[2] X.B. Chen, S.H. Shen, L.J. Guo, S.S. Mao, Chemical Reviews 110 (2010) 6503–6570.
[3] A. Fihri, V. Artero, M. Razavet, C. Baffert, W. Leibl, M. Fontecave, Angewandte Chemie International Edition 47 (2008) 564–567.
[4] X. Zong, H. Yan, G. Wu, G. Ma, F. Wen, Lu. Wang, C. Li, Journal of the American Chemical Society 130 (2008) 7176–7177.
[5] E. Bae, W. Choi, Journal of Physical Chemistry B 110 (2006) 14792–14799.
[6] J. Kim, W.Y. Choi, Energy and Environmental Science 3 (2010) 1042–1045.
[7] V. Daskalaki, G.D. Kondarides, Environmental Science and Technology 44 (2010) 7200–7205.
[8] A. Fujishima, T.N. Rao, D.A. Tryk, Journal of Photochemistry and Photobiology C 1 (2000) 1–21.
[9] M.R. Hoffmann, S.T. Martin, W.Y. Choi, D.W. Bahnemannt, Chemical Reviews 95 (1995) 69–96.
[10] J.C. Yu, J. Yu, W.K. Ho, L.Z. Zhang, Chemistry of Materials 14 (2002) 3808–3816.
[11] A.S. Qaradawi, S.R. Salman, Journal of Photochemistry and Photobiology A 148 (2002) 161–168.
[12] J.G. Yu, Y.R. Su, B. Cheng, Advanced Functional Materials 17 (2007) 1984–1990.
[13] J.G. Yu, L.J. Zhang, B. Cheng, Y.R. Su, Journal of Physical Chemistry C 111 (2007) 10582–10589.
[14] J.G. Yu, W.G. Wang, B. Cheng, B.L. Su, Journal of Physical Chemistry C 113 (2009) 6743–6750.
[15] H.X. Li, J.X. Li, Y.N. Huo, Journal of Physical Chemistry B 110 (2006) 1559–1565.
[16] J. Zhu, J. Ren, Z.F. Bian, H.X. Li, Journal of Physical Chemistry C 111 (2007) 18965–18969.
[17] Z.F. Bian, J. Zhu, S.H. Wang, Y. Cao, X.F. Qian, H.X. Li, Journal of Physical Chemistry C 112 (2008) 6258–6262.
[18] J.C. Yu, W.K. Ho, J.G. Yu, H.Y. Yip, P.K. Wong, J.C. Zhao, Environmental Science and Technology 39 (2005) 1175–1179.
[19] H.G. Yang, H.C. Zeng, Journal of Physical Chemistry B 108 (2004) 3492–3495.
[20] S. Sato, Chemical Physics Letters 123 (1986) 126–128.
[21] H. Irie, Y. Watanabe, K. Hashimoto, Journal of Physical Chemistry B 107 (2003) 5483–5486.
[22] C. Burda, Y. Lou, X. Chen, C.S. Samia, J. Stout, J.L. Gole, Nano Letters 42 (2003) 403–407.
[23] H.X. Li, Z.F. Bian, J. Zhu, D.Q. Zhang, G.S. Li, Y.N. Huo, H. Li, Y.F. Lu, Journal of the American Chemical Society 129 (2007) 8406–8407.
[24] Z.F. Bian, J. Zhu, F.L. Cao, Y.N. Huo, Y.F. Lu, H.X. Li, Chemical Communications 46 (2010) 8451–8453.
[25] X.Q. Gong, A. Selloni, Journal of Physical Chemistry B 109 (2005) 19560–19562.
[26] H.G. Yang, C.H. Sun, S.Z. Qiao, J. Zou, G. Liu, S.C. Smith, H.M. Cheng, G.Q. Lu, Nature 453 (2008) 638–641.
[27] X.G. Han, Q. Kuang, M.S. Jin, Z.X. Xie, L.S. Zheng, Journal of the American Chemical Society 131 (2009) 3152–3153.
[28] H. Yu, B.Z. Tian, J.L. Zhang, Chemistry – A European Journal 17 (2011) 11432–11436.
[29] F. Zuo, L. Wang, T. Wu, Z.Y. Zhang, D. Borchardt, P.Y. Feng, Journal of the American Chemical Society 132 (2010) 11856–11857.
[30] F. Zuo, K. Bozhilov, R.J. Dillon, L. Wang, P. Smith, X. Zhao, C. Bardeen, P.Y. Feng, Angewandte Chemie International Edition 51 (2012) 6223–6226.
[31] M.Y. Xing, J.L. Zhang, F. Chen, B.Z. Tian, Chemical Communications 47 (2011) 4947–4949.
[32] M.Y. Xing, D.Y. Qi, J.L. Zhang, F. Chen, Chemistry – A European Journal 17 (2011) 11432–11436.
[33] G. Liu, H.G. Yang, X.W. Wang, L.N. Cheng, J. Pan, G.Q. Lu, H.M. Cheng, Journal of the American Chemical Society 131 (2009) 12868–12869.
[34] L.M. Qi, J.G. Yu, M. Jaroniec, Physical Chemistry Chemical Physics 13 (2011) 8915–8923.
[35] J. Zhu, J. Yang, Z.F. Bian, J. Ren, Y.M. Liu, Y. Cao, H.X. Li, H.Y. He, K.N. Fan, Applied Catalysis B 76 (2007) 82–91.
[36] Y.N. Huo, Y. Zhang, J. Zhu, H.X. Li, Chemical Communications 47 (2011) 2089–2091.
[37] Y.N. Huo, X.Y. Zhang, Y. Jin, J. Zhu, H.X. Li, Applied Catalysis B 83 (2008) 78–84.
[38] H.X. Li, X. Zhang, Y.N. Huo, J. Zhu, Environmental Science and Technology 41 (2007) 4410–4414.
[39] J. Zhu, S.H. Wang, Z.F. Bian, S.H. Xie, C.L. Cai, J.G. Wang, H.G. Yang, H.X. Li, CrystEngComm 12 (2010) 2219–2224.
[40] J.G. Yu, L.F. Qi, M. Jaroniec, Journal of Physical Chemistry C 114 (2010) 13118–13125.
[41] X.B. Chen, L. Liu, P.Y. Yu, S.S. Mao, Science 331 (2011) 746–750.
[42] R. Sasikala, A. Shirole, V. Sudarsan, T. Sakuntala, C. Sudakar, R. Naik, S.R. Bharadwaj, International Journal of Hydrogen Energy 34 (2009) 3621–3630.
[43] G. Liu, H.G. Yang, X.W. Wang, L.N. Cheng, H.F. Lu, L.Z. Wang, G.Q. Lu, H.M. Cheng, Journal of Physical Chemistry C 113 (2009) 21784–21788.
[44] D.C. Cronemeyer, Physical Review 113 (1959) 1222–1226.
[45] C.P. Kumar, N.O. Gopal, T.C. Wang, M.S. Wong, S.C. Ke, Journal of Physical Chemistry B 110 (2006) 5223–5229.
[46] I. Justicia, P. Ordejon, G. Canto, J.L. Mozos, J. Fraxedes, G.A. Battiston, R. Gerbasi, A. Figueras, Advanced Materials 14 (2002) 1399–1402.
[47] J.C. Conesa, J. Soria, Journal of Physical Chemistry 86 (1982) 1392–1395.
[48] A.A. Ismail, D.W. Bahnemann, Journal of Materials Chemistry 21 (2011) 11686–11707.
[49] X. Li, J. Zhu, H.X. Li, Applied Catalysis B 123–124 (2012) 174–181.